

Structural Determination of Multilayer Graphene via Atomic Moiré Interferometry

David L. Miller,¹ Kevin D. Kubista,¹ Gregory M. Rutter,² Ming Ruan,¹ Walt A. de Heer,¹ Phillip N. First,¹ and Joseph A. Stroscio²

¹School of Physics, Georgia Institute of Technology, Atlanta GA, 30332

²Center for Nanoscale Science and Technology, National Institute of Standards and Technology, Gaithersburg MD, 20899

Rotational misalignment of two stacked honeycomb lattices produces a moiré pattern that is observable in scanning tunneling microscopy as a small modulation of the apparent surface height. This is known from experiments on highly-oriented pyrolytic graphite. Here, we observe the combined effect of three-layer moiré patterns in multilayer graphene grown on SiC(000̄1). Small-angle rotations between the first and third layer are shown to produce a “double-moiré” pattern, resulting from the interference of moiré patterns from the first three layers. These patterns are strongly affected by relative lattice strain between the layers. We model the moiré patterns as a beat-period of the mismatched reciprocal lattice vectors and show how these patterns can be used to determine the relative strain between lattices, in analogy to strain measurement by optical moiré interferometry.

I. INTRODUCTION

Perfect graphene is a single atomic layer of carbon atoms arranged into two interpenetrating triangular sublattices (A & B). It has a unique linear band structure stemming from the unperturbed π orbitals, which lie above the plane of hybridized sp^2 bonds.¹ When placed on a substrate, the band structure may be modified by interaction of the π orbitals with the substrate. One way to minimize this interaction is to use graphene as its own substrate. In Bernal stacked (AB) bilayer graphene, the low-energy band structure near the Fermi energy is not linear due to a breaking of the sublattice symmetry; however, if the layers are rotated away from Bernal stacking the sublattice symmetry and linear band dispersion is preserved over the unit cell of the newly formed moiré superlattice.²

In addition to affecting the electronic structure, the moiré pattern resulting from lattice misalignment or mismatch can itself be a useful tool for understanding structural properties. Optical moiré interferometry has been applied in strain analysis for many years.³ Because a scanning tunneling microscope (STM) can detect moiré patterns in rotated graphene layers,⁴ analogous methods can be applied to measure local strains between individual sheets of graphene at the nanometer scale. Here we show how STM-based “atomic moiré interferometry” can go beyond surface properties to detect lattice orientations and strains for depths of several layers. We expect this type of analysis to be beneficial to understanding electronic and transport properties in graphene multilayers.

Over the past 20 years, several studies of moiré patterns occurring on highly-oriented pyrolytic graphite (HOPG) have been conducted.^{5–10} These typically occur due to a rotation between two layers near the surface, or from an exfoliated flake resting on the HOPG surface.¹¹ Graphene islands grown on transition metal surfaces (e.g., Ir(111), Ru(0001), or Pd(111))^{12–14} also display moiré-style superlattices due to both rotational misalignment and the inherent size mismatch of the lattices. More recently, it was found that multilayer epitaxial graphene (MEG) grown on SiC(000̄1) stacks in such a way that almost every pair of graphene sheets is rotated with respect to its neighbor(s). Graphitic Bernal stacking of the graphene layers appears to be rare in this material,

although there are clearly preferred layer orientations.^{2,4,15} X-ray diffraction and low-energy electron diffraction experiments show broad peaks corresponding to rotations of $\pm 2.2^\circ$ and 30° to the SiC lattice.^{2,4} The rotational disorder of the graphene samples produces moiré patterns in STM topographs, and has been under active investigation.^{2,4,16–19} The patterns appear as an additional corrugation in STM imaging; however, the apparent height variation is thought to be dominated by a modulation in the local density of states.^{7,20} The local stacking changes continuously between regions that resemble AA, AB, BA and slip stacking.⁷ Despite regions of locally AB stacking, the sublattice symmetry is preserved over the full moiré unit cell. In each unit cell, AB regions are complemented by BA regions that restore the inversion symmetry. The result is that the electronic properties of an N -layer film of MEG are nearly equivalent to N independent graphene layers: the linear band dispersion near the charge neutrality (Dirac) points of the Brillouin zone is preserved.^{2,15,21}

II. EXPERIMENTAL METHODS

Multilayer graphene is grown on SiC(000̄1) by a low-vacuum induction furnace technique.^{22,23} When heated, the SiC crystal thermally decomposes leaving behind carbon atoms to reform into graphene sheets. The sample studied has an average of 10 ± 1 layers as measured by ellipsometry. It was initially imaged using atomic force microscopy (AFM) and inspected with low energy electron diffraction (LEED) and Auger electron spectroscopy (AES) to ensure the sample quality. The sample was then placed into a custom built ultra-high vacuum chamber (base pressure $< 10^{-9}$ Pa), where it was subsequently heated to 1250°C in order to clean the surface after exposure to air. After cleaning, it was studied at low temperature (4.3 K) in a cryogenic STM chamber.²¹

III. MULTILAYER MOIRÉ

Multilayer graphene often yields more complicated moiré patterns than HOPG, resulting from the successive rotation of layers throughout the depth of the material. Multiple moiré

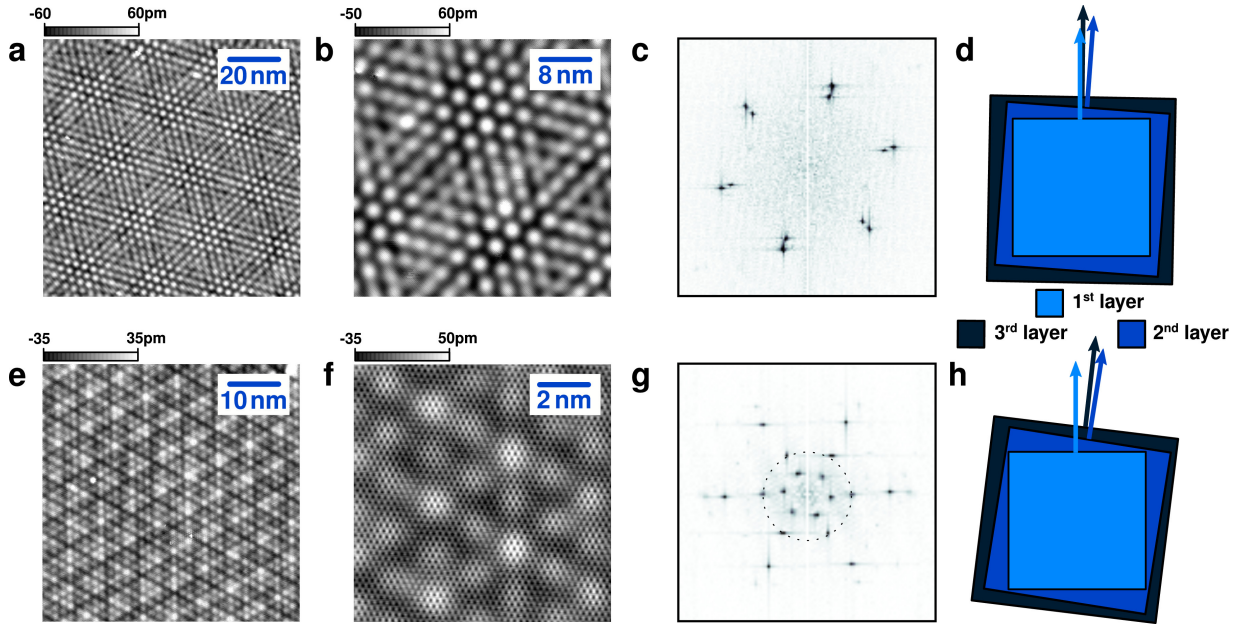


FIG. 1: Comparison of two moiré patterns in MEG showing multiple layer effects. (a) An image of two similar sized moiré patterns interfering, resulting in a large unit cell pattern. Layers 1 (Surface Layer) and 2, and 2 and 3 have comparable rotation angles in opposite directions (shown in d). (b) zoomed in view of (a). (c) FT of (a). (d) schematic of layer orientation based on the moiré pattern in (a). (e) A different superstructure that indicates low rotation angles between layers 2 and 3. The spots in the FT relative to the reciprocal lattice vectors were used in this case to determine which spots correspond to the rotation between layer 1 and 2. (f) zoomed in view of (e). (g) FT of (e). (h) schematic of layer orientation based on the moiré pattern in (e).

patterns are often seen during imaging (Figure 1). Unlike HOPG, Bernal stacking does not frequently occur; thus, sub-surface layers will also have moiré alignment, which can be observed. Various publications have reported an attenuation factor (AF) associated with overlayer coverage of a moiré pattern in HOPG.^{8,9,24} A fit of this data yields $AF_n = e^{-0.81n}$, where n is the number of overlayers.¹⁰ In view of this, a second/third layer moiré pattern would be visible ($AF_1 = 2.25$) if present but the visibility of patterns from deeper layers decays exponentially.

The length of a superlattice cell can be evaluated as the wavelength of an interference pattern resulting from the misaligned reciprocal lattice vectors. The difference between a reciprocal lattice vector \mathbf{k}_i and a reciprocal lattice vector rotated by angle θ , $\mathbf{k}'_i = \hat{R}(\theta)\mathbf{k}_i$, is used to determine the length (D) and orientation (ϕ) of the pattern. Since we are interested in long wavelength moiré patterns (rotation angles, $\theta \leq 5^\circ$), the only relevant vectors of the interference pattern will be $\Delta\mathbf{k} = \mathbf{k}_i - \mathbf{k}'_j$ for $i = j$ where i is any of six reciprocal lattice vectors. For unstrained lattices, only one pair of vectors \mathbf{k} and \mathbf{k}' needs to be considered because of symmetry. Thus, for two rotated lattices of undistorted length, we obtain the equation for the size of the moiré unit cell length^{5,25}

$$D = \frac{2\pi}{|\mathbf{k} - \mathbf{k}'|} = \frac{a}{2 \sin(\theta/2)}, \quad (1)$$

and orientation with respect to the atomic lattice,

$$\phi = \frac{\pi}{6} - \theta/2. \quad (2)$$

Figure 1a shows an example of two interfering moiré patterns (the collective interference of three graphene layers), obtained by STM measurements. On first glance, one might think that the moiré pattern constitutes a significant modulation in the tip height. In fact, the graphene lattice is extremely smooth, such that any small changes in tip height become the foremost feature. Height modulations due to moiré patterns are typically only 0.05 nm peak-to-peak. From Fig. 1a and Fig. 1b, two periodicities can be seen. The large periodicity has a length of $D \approx 26.5$ nm while the smaller periodicity has a length of $D \approx 3$ nm, still much larger than the atomic lattice spacing. Because more than a single moiré pattern is observed, we can conclude that this is a combined effect of at least three layers (in another area of the sample, 3 coexisting moiré patterns were found, implying the participation of at least 4 graphene layers). From the discrete fast Fourier transform (FT) in Fig. 1c, we find that two sets of spots are present in reciprocal space. These spots correspond to moiré lengths of $D_1 = 2.95 \pm 0.05$ nm and $D_2 = 3.35 \pm 0.09$ nm.²⁶

Using equations (1) and (2) and $a = 0.246$ nm as the graphene lattice constant, we deduce the rotation angles needed to produce a moiré of size D_1 and D_2 as $\theta_1 = 4.78 \pm 0.07^\circ$ and $\theta_2 = 4.21 \pm 0.11^\circ$. Because $\Delta\phi = \phi_1 - \phi_2 \approx 0^\circ$, as seen in the Fourier transform, we propose the orientation of the top three layers in Fig. 1d. The first and third layers (starting from the surface and counting into the bulk) must be nearly aligned in order to obtain the observed $\Delta\phi$ in the FT. The measured value is $\Delta\phi = 0.61 \pm 0.23^\circ$, slightly higher than the expected value of $\Delta\phi = 0.29^\circ$ from the proposed three

layer orientation (Fig. 1d) and equation (2).²⁶ Again, we can determine the length of the largest interference pattern from $\Delta\mathbf{k}$ using the moiré reciprocal lattice vectors from the FT,

$$D_3 = \frac{D_1 D_2}{\sqrt{D_1^2 + D_2^2 - 2D_1 D_2 \cos(\Delta\phi)}}. \quad (3)$$

Thus, we calculate a value of $D_3 = 24.7 \pm 1.6$ nm for the size of the largest observed pattern.²⁶ The uncertainty is due to a distortion in the hexagonal shape of the pattern, and is likely caused by strain, which will be discussed later. As shown in the schematic in Fig. 1d, the top layer is nearly aligned with the third. This creates two patterns of nearly equal size and orientation. The angle between the two moiré patterns is small, producing a large interference pattern.

In the case of Fig. 1e, we have applied a similar analysis to determine the orientation of the top three lattices. The smallest \mathbf{k} vectors in Fig. 1f were determined to correspond to the moiré pattern of the first and second layers by comparing the moiré pattern orientation with respect to the reciprocal lattice vectors. We propose that there is a small rotation between the second and third layer. The interference of these two moiré patterns is responsible for the hexagonal set of spots on the dotted circle in the FT (Fig. 1g). Consequently, the image in Fig. 1e looks qualitatively very different than the one in Fig. 1a.

As further proof of concept, we image the pattern at multiple sample biases for a constant tunneling current. Because the imaging is done in a constant current mode, the tip will move closer to the surface as the sample bias (V_S) is decreased. This technique is used in imaging Bernal stacked graphene bilayers, and shows a transition in the imaging of the atomic lattice.²⁷ At higher biases, every atom is imaged; however, as the bias is decreased the tip instead images every other atom.

Figures 2(a-d) show the result of imaging at multiple biases on a region within the image shown in Fig. 1a. At $V_S = -0.5$ V, a single set of moiré maxima is seen, corresponding to a moiré pattern from the rotation of the first/second layer. As the bias decreases, the tip begins to image a second moiré pattern. By $V_S = -0.05$ V, the tip images only the second moiré pattern, which apparently results from rotation of layers 2 and 3. From measured deviations in the expected exponential decay of tunneling current vs tip-height (I vs z), we believe that by $V_S = -0.05$ V the tip is in contact with the surface. The difference in tip height between $V_S = -0.5$ V and $V_S = -0.05$ V is $\Delta z = 0.39$ nm. The sample biases at $V_S = -0.3$ V, -0.2 V (Fig. 2b,c) show the transition in imaging the top moiré to the one underneath. The tip bias, tunneling current and tip shape are known to have a large effect on the imaging of a moiré pattern.¹⁰ This behavior was calculated for a rotated layer on top of AB stacked graphite²⁸ and effects similar to our own observations were predicted; however, at present we do not understand how the moiré patterns of this multilayer system depend on tip-sample distance.

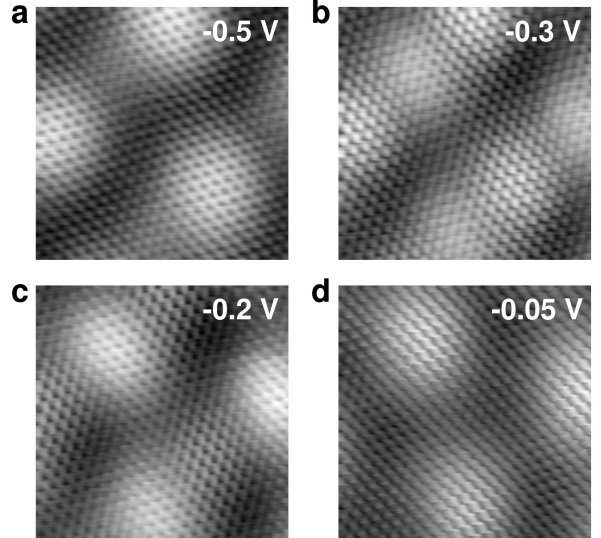


FIG. 2: Multibias imaging on the moiré pattern in Figure 1a. Each image is $5 \text{ nm} \times 5 \text{ nm}$, and was taken at the same spatial location and tunnel current (100 pA). In (a), only the moiré pattern of the top two layers is imaged. (b), (c) show the transition as the tip moves closer to the surface. In (d), the tip has pushed in far enough to only image the lower layer moiré pattern. We believe that by $V_S = -0.05$ V, the tip is actually in contact with the surface.

IV. STRAIN

Relative strain induced between two stacked hexagonal lattices can have a large effect on observed superlattice wavelengths. This phenomenon is well known in moiré interferometry as a technique for strain measurement,³ and has been observed in large period moiré patterns on HOPG.⁶ The effect appears as a distortion in the real space hexagonal shape of the superlattice cell, resulting from unequal distortion of both the relative length and angular alignment of the reciprocal lattice vectors. Distorted moiré patterns are commonly observed in HOPG when lattice rotation angles (θ) are small. We examine the effect of a uniform strain in the top layer relative to an unstrained layer below. For simplicity, we demonstrate the effect of a relative strain in the arm chair direction on the observed superlattice periodicity.

Strain breaks the symmetry of the reciprocal lattice vectors, so we now consider the case where the lattice has been uniformly strained along the arm chair direction, such that $|\mathbf{a}'_i| = (1 + \epsilon_i)|\mathbf{a}_i|$, where $i = 0, \pm$. The vector \mathbf{k}_0 along the direction of strain does not change angular orientation ($\varphi_0 = 0$), so under rotation

$$\mathbf{k}'_0 = \frac{1}{(1 + \epsilon_0)} \hat{R}(\theta) \mathbf{k}_0. \quad (4)$$

This leads to a change in the wavelength of the interference pattern along the strain direction as given by the law of

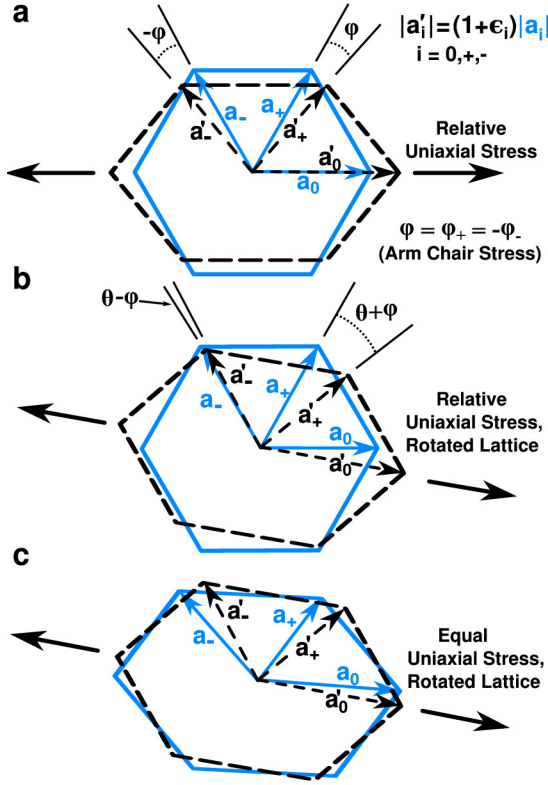


FIG. 3: Strain induced between two stacked hexagonal (real space) lattices in the case where one lattice (black/dashed line) is (a) stretched but not rotated and (b) stretched and rotated with respect to the undistorted lattice (blue/solid line). (c) displays equal strain for both lattices. For rotated lattices under relative strain, the angular change in the lattice vectors affect the interference pattern differently for each direction. As a result, the moiré pattern observed in STM will appear stretched or distorted. Significantly higher strain is required for similarly sized distortions if the lattices are equally strained along the same direction. At the low moiré angles (θ), the lattice vectors (when equally strained) will obtain similarly sized angular distortions φ_i which will nullify each other.

cosines,

$$D_0 = \frac{2\pi}{|\mathbf{k}_0 - \mathbf{k}'_0|} = \frac{a(1 + \epsilon_0)}{2\sqrt{(1 + \epsilon_0)\sin^2(\theta/2) + \epsilon_0^2/4}}, \quad (5)$$

Lattice vectors (\mathbf{a}_\pm) which are not along the direction of strain will undergo an additional rotation, φ_\pm . In the most general case of arbitrary changes in length (ϵ_i) and arbitrary rotations (φ_i), this becomes:

$$D_i = \frac{2\pi}{|\mathbf{k}_i - \mathbf{k}'_i|} = \frac{a(1 + \epsilon_i)}{2\sqrt{(1 + \epsilon_i)\sin^2[(\theta + \varphi_i)/2] + \epsilon_i^2/4}}. \quad (6)$$

where $i = 0, \pm$, and the distortion in the angular orientation of the moiré is given by

$$\phi_i = \arcsin \left(\frac{(1 + \epsilon_i)\sin(\theta + \varphi_i)}{2\sqrt{(1 + \epsilon_i)\sin^2[(\theta + \varphi_i)/2] + \epsilon_i^2/4}} \right) \quad (7)$$

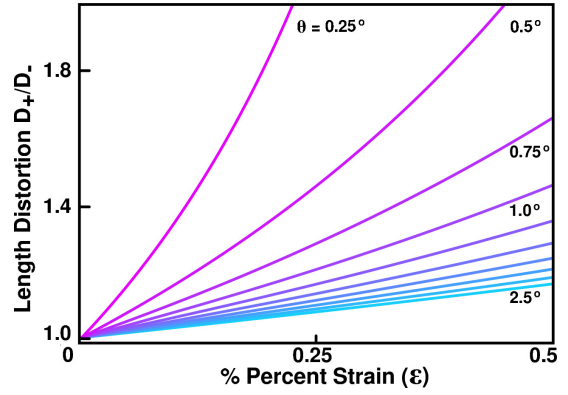


FIG. 4: Curves display the length distortion between two vectors of the moiré cell as a function of the moiré rotation angle θ . The amount of distortion for a small strain rapidly increases with decreasing moiré rotation angles (i.e. when the rotation angle is comparable to the angular distortion, $\theta \sim \varphi$).

In order to approximate the values of ϵ_i for a uniform uniaxial stress, we make use of Poisson's ratio ν and the strain matrix $\boldsymbol{\epsilon}$ by, $\epsilon_x = \epsilon$, $\epsilon_y = -\nu\epsilon$.²⁹ The strain matrix is:

$$\boldsymbol{\epsilon} = \begin{pmatrix} 1 + \epsilon & 0 \\ 0 & 1 - \nu\epsilon \end{pmatrix}, \quad (8)$$

where the axes have been chosen to diagonalize the strain matrix. For strain in the arm chair direction, we do not need to rotate the lattice vectors \mathbf{a}_i with respect to $\boldsymbol{\epsilon}$. In this case the lattice is stressed along \mathbf{a}_0 . We can relate the strain matrix to the values ϵ_i by applying the original definition,

$$|\mathbf{a}'_i| = (1 + \epsilon_i)|\mathbf{a}_i| = |\boldsymbol{\epsilon}\mathbf{a}_i|. \quad (9)$$

Thus, under a small strain approximation ($\epsilon \ll 1$) we obtain

$$\epsilon_0 = \epsilon, \epsilon_{\pm} \approx \frac{1}{4}(1 - 3\nu)\epsilon. \quad (10)$$

$$\varphi_0 = 0, \varphi_{\pm} \approx \pm \sqrt{3}\epsilon \left| \frac{1 + \nu}{4 + \epsilon(1 - 3\nu)} \right| \quad (11)$$

We use the values from equations (10) and (11), along with $\nu = 0.5$ to plot the overall distortion in the wavelength of the interference pattern. If we put these values into (6), we can compare the length distortion (D_+/D_-) of the resulting moiré pattern. Figure 4 clearly shows the expected behavior. As the rotation angle θ between the lattices increases, the effect of the distortion is quickly diminished; however, for a large moiré pattern the rotation angle is small, leaving the pattern easily distorted by the relative strain. The reason is that small angular differences become comparable to the rotation angle ($\varphi \approx \theta$), and lattice distortions cannot be neglected. Additionally, in this regime small changes in the lattice constant a contribute greatly to the moiré rotation angle. The shape of the moiré hexagon suffers additional skewing in ϕ_i due to the angular distortion of the reciprocal lattice vectors.

Obtaining an exact measure of the strain is difficult because it can be hard to determine the direction of the applied stress.

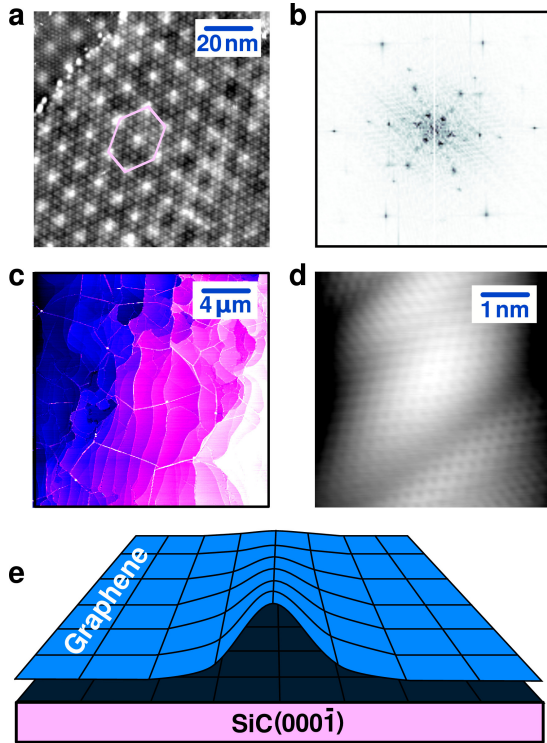


FIG. 5: (a) An image of how strain can affect a moiré pattern. (b) displays the FT of the image in (a). As many as 5 sets of moiré spots can be identified, requiring interactions from at least 4 layers. Strain can be caused by low angle grain boundaries seen in (a) or “pleats”. The AFM image in (c) shows these structures. The pleats are folds in the graphene lattice and tend to run along the SiC step or at angles roughly perpendicular to them. The STM image in (d) shows atomic imaging on top of a pleat. (e) Schematic of a pleat in epitaxial graphene. Mismatches in the thermal contraction after growth can induce buckling in the lattice.

Distortions can also be made from equally stretching both lattices along one direction as in Fig. 3c; however the distortions of the resulting moiré patterns are generally much smaller than for relative strains (on the order of several percent strain for a comparable length distortion). The reason is that for small moiré rotation angles, the lattice vectors will obtain similarly sized angular distortions for each lattice vector pair, i , thereby yielding a relative angular distortion of $\varphi_i - \varphi'_i \approx 0$. In this case, we can use the original moiré equations to approximate the length distortion simply by replacing the lattice spacing a in equation (1) with its distorted values, $a_i = (1 + \epsilon_i)a$.

Given a low enough angle rotation, the relative strain effects are indeed observed. Low angle moiré patterns are even more likely to occur when multiple patterns can be simultaneously observed. Figure 5a shows a fairly large moiré pattern with an average unit cell length of $D = 10.5 \text{ nm} \pm 0.9 \text{ nm}$, corresponding to a rotation angle $\theta = 1.36 \pm 0.11^\circ$; however, distortion from relative strain causes the actual size of the moiré pattern to range from 9.50 nm to 11.7 nm, depending on which axis is

measured.²⁶ This corresponds to a moiré length distortion of 23% ($D_{\max}/D_{\min} = 11.7/9.50 = 1.23$); thus we estimate the parameter $\varepsilon \approx 0.37\%$ for the relative strain between the two lattices producing the pattern.

There are a few mechanisms by which a graphene sheet can undergo strain. In Fig. 5a, low angle grain boundaries are visible. The moiré pattern bends with the boundary on the right. In this case, the subsurface rippling of the lattice is likely causing a slight relative strain. Another type of strain possible in graphene grown on SiC(000̄1) is a bending of the graphene sheet caused by unequal thermal contractions between the SiC and graphene sheets after growth.³⁰ In order to relieve stress, the lattice buckles (see Fig. 5e). The image in Fig. 5c was taken by atomic force microscopy, and shows these “pleats” of the graphene sheet. They are typically 5 nm to 10 nm in height, and are visible in Fig. 5c as white lines running parallel and transverse to the SiC steps. Despite bending, the graphene lattice stays in tact over a pleat, and the graphene lattice can extend for several microns before a pleat occurs. The STM image in Fig. 5d was taken on top of a graphene pleat. The lattice is continuous, but it is clearly contorted as a result of the lattice buckling. The strain relief looks much like the strain relief in nanotubes.³¹ Flat areas near these pleats could show strain effects. Immediately around pleats, slight layer delamination is possible which may not even produce a recognizable moiré pattern to be observed.

V. CONCLUSIONS

Multilayer epitaxial graphene is known to have carrier mean free times comparable to suspended monolayer graphene,^{21,32,33} and measurements to date indicate that its electronic structure is effectively that of independent graphene monolayers.^{15,34} However, the physical structure of MEG is complex. Using the methods developed here, surface STM imaging can be used to obtain layer alignments and local strain from at least 3 graphene layers in the multilayer stack. These microscopic measurements will be useful for deciphering the formation of rotational domains and for mapping inhomogeneous strain fields, each of which could affect the quantum states of this material—especially under the influence of electric and magnetic fields.

Acknowledgments

We thank C. Berger, M. Sprinkle, N. Sharma, S. Blankenship, A. Band, and F. Hess for their technical contributions to this work. Funding from NSF (DMR-0804908), the Semiconductor Research Corporation Nanoelectronics Research Initiative (NRI-INDEX), and the W. M. Keck Foundation are gratefully acknowledged. Graphene production facilities were developed under NSF grant ECCS-0521041.

¹ P. R. Wallace, Phys. Rev. **71**, 622 (1947).

² J. Hass, F. Varchon, J. E. Millán-Otoya, M. Sprinkle, N. Sharma, W. A. de Heer, C. Berger, P. N. First, L. Magaud, and E. H. Conrad, Phys. Rev. Lett. **100**, 125504 (2008).

³ R. H. Bromley, Proceedings of the Physical Society. Section B **69**, 373 (1956).

⁴ J. Hass, W. A. de Heer, and E. H. Conrad, J. Phys.: Condens. Matter **20**, 323202 (2008).

⁵ M. Kuwabara, D. R. Clarke, and D. A. Smith, Appl. Phys. Lett. **56**, 2396 (1990).

⁶ J. Xhie, K. Sattler, M. Ge, and N. Venkateswaran, Phys. Rev. B **47**, 15835 (1993).

⁷ Z. Y. Rong and P. Kuiper, Phys. Rev. B **48**, 17427 (1993).

⁸ Z. Y. Rong, Phys. Rev. B **50**, 1839 (1994).

⁹ H.-L. Sun, Q.-T. Shen, J.-F. Jia, Q.-Z. Zhang, and Q.-K. Xue, Surf. Sci. **542**, 94 (2003).

¹⁰ W.-T. Pong and C. Durkan, J. Phys. D **38**, R329 (2005).

¹¹ Y. Gan, W. Chu, and L. Qiao, Surface Science **539**, 120 (2003).

¹² S. Marchini, S. Günther, and J. Wintterlin, Phys. Rev. B **76**, 075429 (2007).

¹³ A. T. N'Diaye, J. Coraux, T. N. Plasa, C. Busse, and T. Michely, New J. Phys. **10**, 043033 (16pp) (2008).

¹⁴ S.-Y. Kwon, C. V. Ciobanu, V. Petrova, V. B. Shenoy, J. Bareño, V. Gambin, I. Petrov, and S. Kodambaka, Nano Lett. **9**, 3985 (2009).

¹⁵ M. Sprinkle, D. Siegel, Y. Hu, J. Hicks, A. Tejeda, A. Taleb-Ibrahimi, P. LeFèvre, F. Bertran, S. Vizzini, H. Enriquez, S. Chiang, P. Soukiasian, C. Berger, W. A. de Heer, A. Lanzara, and E. H. Conrad, Phys. Rev. Lett. **103**, 226803 (2009).

¹⁶ M. Naithoh, M. Kitada, S. Nishigaki, N. Toyama, and F. Shoji, Surf. Rev. Lett. **10**, 473 (2003).

¹⁷ F. Varchon, P. Mallet, L. Magaud, and J.-Y. Veuillen, Phys. Rev. B **77**, 165415 (2008).

¹⁸ L. B. Biedermann, M. L. Bolen, M. A. Capano, D. Zemlyanov, and R. G. Reifenberger, Phys. Rev. B **79**, 125411 (2009).

¹⁹ F. Hiebel, P. Mallet, F. Varchon, L. Magaud, and J.-Y. Veuillen, Phys. Rev. B **78**, 153412 (2008).

²⁰ J. M. Campanera, G. Savini, I. Suarez-Martinez, and M. I. Heggie, Phys. Rev. B **75**, 235449 (2007).

²¹ D. L. Miller, K. D. Kubista, G. M. Rutter, M. Ruan, W. A. de Heer, P. N. First, and J. A. Stroscio, Science **324**, 924 (2009).

²² C. Berger, Z. Song, T. Li, X. Li, A. Y. Ogbazghi, R. Feng, Z. Dai, A. N. Marchenkov, E. H. Conrad, P. N. First, and W. A. de Heer, J. Phys. Chem. B **108**, 19912 (2004).

²³ C. Berger, Z. Song, X. Li, X. Wu, N. Brown, C. Naud, D. Mayou, T. Li, J. Hass, A. N. Marchenkov, E. H. Conrad, P. N. First, and W. A. de Heer, Science **312**, 1191 (2006).

²⁴ W.-T. Pong, J. Bendall, and C. Durkan, Jpn. J. Appl. Phys. **44**, 5443 (2005).

²⁵ I. Amidror, J. Opt. Soc. Am. A **20**, 1900 (2003).

²⁶ All uncertainties reported represent one standard deviation in the measured quantity. Error is calculated from the position of the intensity spots of the FT.

²⁷ G. M. Rutter, J. N. Crain, N. P. Guisinger, P. N. First, and J. A. Stroscio, J. Vac. Sci. Technol. **26**, 938 (2008).

²⁸ E. Cisternas, M. Flores, and P. Vargas, Phys. Rev. B **78**, 125406 (2008).

²⁹ C. Kittel, *Introduction to Solid State Physics*, 7th ed. (John Wiley and Sons, New York, NY, USA, 1996), pp. pp. 80–95.

³⁰ Z. G. Cambaz, G. Yushin, S. Osswald, V. Mochalin, and Y. Gogotsi, Carbon **46**, 841 (2008).

³¹ D. Orlikowski, M. Buongiorno Nardelli, J. Bernholc, and C. Roland, Phys. Rev. B **61**, 14194 (2000).

³² M. Orlita, C. Faugeras, P. Plochocka, P. Neugebauer, G. Martinez, D. K. Maude, A.-L. Barra, M. Sprinkle, C. Berger, W. A. de Heer, and M. Potemski, Phys. Rev. Lett. **101**, 267601 (2008).

³³ K. I. Bolotin, F. Ghahari, M. D. Shulman, H. L. Stormer, and P. Kim, Nature **462**, 196 (2009).

³⁴ M. Sadowski, G. Martinez, M. Potemski, C. Berger, and W. de Heer, Solid State Communications **143**, 123 (2007).